

ECCENTRIC JUPITERS VIA DISK-PLANET INTERACTIONS

PAUL C. DUFFELL AND EUGENE CHIANG

Department of Astronomy and Theoretical Astrophysics Center, University of California, Berkeley
Draft version December 7, 2024

ABSTRACT

Numerical hydrodynamics calculations are performed to determine conditions under which giant planet eccentricities can be excited by parent gas disks. Unlike in other studies, Jupiter-mass planets are found to have their eccentricities amplified — provided their orbits start eccentric. We disentangle the web of co-rotation, co-orbital, and external resonances to show that this finite-amplitude instability is consistent with that predicted analytically. Ellipticities can grow until they reach of order the disk’s aspect ratio, beyond which the external Lindblad resonances that excite eccentricity are weakened by the planet’s increasingly supersonic epicyclic motion. Forcing the planet to still larger eccentricities causes catastrophic eccentricity damping as the planet collides into gap walls. If the eccentricity driving documented here survives in 3D, it may explain the low-to-moderate eccentricities $\lesssim 0.1$ exhibited by many giant planets (including Jupiter and Saturn), especially those without planetary or stellar companions.

Subject headings: hydrodynamics — planet-disk interactions — planets and satellites: formation — planetary systems: protoplanetary disks

1. INTRODUCTION

One of the most surprising revelations of Doppler exoplanet surveys is the prevalence of Jupiter-mass planets on highly elliptical orbits (e.g., Marcy et al. 2005). At orbital periods $\gtrsim 10$ days, beyond the reach of tidal circularization, giant planet eccentricities span the full gamut from near-zero to near-unity. There is growing evidence that gravitational interactions between planets can explain the extravagant eccentricities observed (e.g., Takeda & Rasio 2005; Jurić & Tremaine 2008; Wu & Lithwick 2011; Dawson & Chiang 2014).

But are planet-planet interactions the whole story? After removing observational biases, a substantial fraction of giant planets have low-to-moderate eccentricities: $\sim 28\%$ have $e < 0.05$ — our solar system gas giants belong to this cohort — and fully half have $e < 0.15$ (Zakamska et al. 2011, see their Figure 11, bottom panel). These statistics are drawn from the single-planet catalog of Butler et al. (2006). Continued Doppler monitoring has not changed the single status of many of these planets, particularly at semimajor axes > 1 AU (Bryan et al., submitted). For solitary giants having no stellar or planetary perturbers in sight, we look instead to their parent gas disks to understand how their ellipticities may have arisen.

Planet-disk interactions are mediated by resonances, of which there are as many kinds as there are terms in the Fourier expansion of the planet’s potential. Some resonances damp eccentricity while others excite it. Goldreich & Sari (2003, hereafter GS03) outlined the circumstances whereby certain resonant interactions could dominate others to excite eccentricity in the net. The planet would need to (1) carve out a gap around its orbit, and (2) have its eccentricity exceed a threshold value, which GS03 estimated to be on the order of a few percent (see Sections 2 and 4.1 for the technical details). Amplification of eccentricity by disk torques could then

proceed, presumably until the planet crashed into the gap walls. Eccentricities excited by disks would then be limited by the fractional radial widths of gaps, of order ~ 0.1 . Planet-disk interactions can thus be argued to be relevant for eccentricities in the range ~ 0.01 – 0.1 .

The finite-amplitude instability of GS03 has seen little if any support in numerical studies. Overwhelmingly, planets the mass of Jupiter or lower are seen in numerical simulations to have their eccentricities damped (e.g., Papaloizou et al. 2001; Cresswell & Nelson 2006; Cresswell et al. 2007; Bitsch & Kley 2010; Dunhill et al. 2013). Many of these studies found that eccentricities grow only for planets of extremely high mass $\gtrsim 20M_J$, via a mechanism that differs from the one proposed by GS03 (see Section 2). To our knowledge, the one numerical study that reported otherwise was by D’Angelo et al. (2006) who found that Jupiter-mass planets could have their eccentricities excited to values of ~ 0.1 . It is unclear whether their results vindicate the GS03 mechanism, as D’Angelo et al. (2006) observed eccentricities to grow starting from zero; in other words, no evidence was found for a finite-amplitude instability.

All previous numerical studies of eccentricity evolution used a “live-planet” approach: the planet’s orbit was free to evolve under the action of disk torques. Although natural enough, a live-planet simulation can be tricky to diagnose because all parameters are in flux. We advocate here a “fixed-planet” methodology: the planet is kept on a fixed eccentric orbit; the disk is allowed to relax to a quasi-steady state (one that oscillates consistently with the epicyclic phase of the planet); and disk forces on the planet are then measured to extract the rate of change of planet eccentricity \dot{e} as a function of e . The fixed-planet approach permits greater control of environmental variables and more systematic exploration of parameter space.

In Section 2 we briefly review the theoretical considerations underlying how disks affect planetary eccentricities. We summarize the tenets of the theory of GS03 and also

itemize aspects of the problem that they did not treat. Section 3 describes the numerical methods we employed to measure $\dot{e}(e)$ for Jupiter-mass planets. Results, including a head-to-head comparison with the predictions of GS03, are given in Section 4. A summary and outlook is contained in Section 5. The Appendix compiles all the formulae we used to test GS03, drawn from several analytic studies.

2. THEORETICAL BACKGROUND

According to GS03, eccentricity excitation requires two ingredients:

- The planet must carve a deep enough gap in the disk — or more accurately, a gap with steep enough density gradients — that first-order (as expanded in the planet’s eccentricity) co-orbital Lindblad resonances situated at the very gap center become weaker than first-order external Lindblad resonances located roughly a gas scale height h away from gap center. The latter drive eccentricity, while the former damp eccentricity. Citing calculations by Artymowicz (1993), GS03 stated that the gap profile must be such that the surface density at the locations of the strongest externals must be greater than the surface density at gap center by at least a factor of ~ 3 for the externals to defeat the co-orbitals.¹
- First-order co-rotation resonances, which also damp eccentricity, must be “saturated” (weakened), meaning that material librating in co-rotation resonance must not be replenished by viscous inflow of fresh material (Ogilvie & Lubow 2003). Saturation is effected for sufficiently large $e > e_{\min}$; in other words, eccentricity excitation is a finite-amplitude instability.

As estimated by GS03, the minimum eccentricity necessary for $\dot{e} > 0$ is

$$e_{\min} \sim \left(\frac{w}{a}\right)^{5/3} \left(\frac{\nu}{\Omega_0 a^2}\right)^{2/3} q^{-1} \quad (1)$$

where q is the planet-to-star mass ratio, a is the planet’s semimajor axis, Ω_0 is the planet’s orbital frequency, w is the gap width, and ν is the kinematic viscosity. To estimate w , GS03 balance the one-sided principal (zeroth-order) Lindblad torque with the local viscous torque

$$q^2 \Omega_0^2 \Sigma a^4 (a/w)^3 \sim \nu \Sigma a^2 \Omega_0 \quad (2)$$

and obtain

$$w/a \sim (q^2/\tilde{\nu})^{1/3} \quad (3)$$

where Σ is the disk surface density and $\tilde{\nu} = \nu/(a^2 \Omega_0)$ is the kinematic viscosity with dimensions scaled out. Equation (2) ignores changes in Σ across the gap which can actually be substantial;² we will, in any case, test

¹ We will find in practice that this requirement is met only for gaps that are extremely deep in the sense that their central surface densities are suppressed by about 3 orders of magnitude relative to the background disk.

² Fung et al. (2014) did account for changes in surface density when writing down (2), deriving a scaling relation for gap depth

scaling relation (3) numerically in Section 4.3. Substituting (3) into (1) gives

$$e_{\min} \sim (q\tilde{\nu})^{1/9}. \quad (4)$$

For our standard parameters of $q = 0.001$ and $\tilde{\nu} = 2.5 \times 10^{-6}$ (corresponding to a Shakura-Sunyaev $\alpha = 0.002$ and disk aspect ratio $h/a = 0.036$), equation (1) — which is not meant to be more than an order-of-magnitude estimate — gives $e_{\min} \sim 0.1$.

For $e > e_{\min}$, a reasonable expectation not specifically discussed by GS03 is that the eccentricity should grow until the planet’s radial epicyclic motion causes it to collide with the gap walls. The maximum eccentricity e_{\max} should then scale as w/a .³

A useful order-of-magnitude formula that gives a sense of scale is the maximum rate of eccentricity damping in the limit of small e and no gap clearing (Artymowicz 1993):

$$\max |\dot{e}/e| \sim q \left(\frac{a}{h}\right)^4 \frac{\Sigma_0 a^2}{M_*} \Omega_0 \quad (5)$$

where Σ_0 is the unperturbed disk density. This maximum rate of eccentricity change is set by the co-orbital resonances. Gap clearing can only reduce the magnitude of eccentricity changes (and potentially change the sign).

Other effects not covered by the linear theory of GS03 include torques exerted by material in the immediate vicinity of the planet, on scales of order the Hill radius. Circumplanetary material (not necessarily bound to the planet) may exert dynamical friction and strongly damp the planet’s eccentricity. Properly modeling circumplanetary flows is challenging and subject to numerical issues such as how the planet’s potential is smoothed and how accretion onto the planet is prescribed. Another nonlinear issue concerns instabilities in deep gaps (Li et al. 2009; Yu et al. 2010; Duffell & MacFadyen 2013; Fung et al. 2014; Kanagawa et al. 2015). If the planet mass is large enough or the viscosity is small enough, then gap walls can steepen to the point of triggering the Rayleigh instability or the Rossby wave instability. Gap walls can shed vortices that can stochastically torque the planet.

Finally, we emphasize that the GS03 mechanism for eccentricity growth does not align with the common view that to drive eccentricity requires near-brown dwarf masses and the dominant influence of the outer 1:3 Lindblad resonance. Papaloizou et al. (2001) and Dunhill et al. (2013) found eccentricity driving only for relatively massive giants ($\gtrsim 20 M_J$); these companions opened such wide and deep gaps that they interacted primarily with their disks via the outer 1:3 resonance, amplifying disk eccentricities which were then backreactively shared with the planet by secular interactions. We will find in the present study that the 1:3 resonance is

that succeeds in reproducing numerical results. These authors replaced the left-hand Σ with Σ_{gap} , the right-hand Σ with the unperturbed value Σ_0 , and w with h to arrive at a fairly accurate formula for $\Sigma_{\text{gap}}/\Sigma_0$. Their argument and GS03’s argument for w as presented here are not obviously compatible.

³ We will present evidence supporting this expectation. Actually, we will find that before w/a comes into play, the disk aspect ratio $h/a < w/a$ becomes relevant. See Section 4.1 on the supersonic weakening of Lindblad resonances and how the weakening leads to e_{\max} .

not essential for eccentricity driving; that it is possible to excite planetary eccentricities even for Jupiter-mass planets, along the lines envisioned by GS03.

3. NUMERICAL METHOD

We address the problem of eccentricity evolution numerically by integrating the 2D (vertically integrated) isothermal hydrodynamic equations:

$$\partial_t \Sigma + \nabla \cdot (\Sigma \vec{v}) = 0 \quad (6)$$

$$\partial_t (\Sigma v_j) + \nabla \cdot (\Sigma \vec{v} v_j + P \hat{x}_j - \nu \Sigma \vec{\nabla} v_j) = -\Sigma \vec{\nabla} \phi \quad (7)$$

$$P = c^2 \Sigma \quad (8)$$

where Σ is surface density, P is pressure, \vec{v} is velocity, ν is the kinematic viscosity, c is the sound speed, and ϕ is the gravitational potential from the planet and central star.

The numerical integration is carried out using the DISCO code (Duffell & MacFadyen 2011, 2012, 2013). DISCO is a moving-mesh hydro code that is tailored for the study of disks. Computational zones are annular wedges that shear past one another to follow the underlying flow. By effectively subtracting off the background Keplerian flow, DISCO can provide an accurate solution for formally supersonic problems, and can integrate for long times.

The numerical domain extends from an inner radius $r_{\text{in}} = 0.4$ to an outer radius $r_{\text{out}} = 2$, with the planet's semimajor axis located at radius $r = a = 1$.⁴ The domain is divided into $N_r = 360$ logarithmically spaced radial zones, corresponding to $\Delta r/r \simeq 0.0045$. The azimuthal resolution varies with radius to ensure grid cells with near-unity aspect ratios, $\Delta r \simeq r \Delta \phi$.

3.1. Disk Model and Planet Potential

A simple background disk is employed that ignores gradients in density Σ , viscosity $\nu \equiv \alpha(h/a)^2$, and sound speed c :

$$\Sigma(r) = \Sigma_0 = 1 \quad (9)$$

$$\Omega(r) = \Omega_0 (r/a)^{-3/2} \quad (10)$$

$$v_r(r) = -\frac{3}{2} \nu / r \quad (11)$$

$$P(r) = c^2 \Sigma_0 \quad (12)$$

$$c = a \Omega_0 / \mathcal{M} \quad (13)$$

where v_r is the background radial accretion velocity and $\mathcal{M} \equiv a/h$ is the constant Mach number, with h the gas scale height.

The gravitational potential at position \vec{x} is that of the star + planet:

$$\phi(\vec{x}) = GM_* \left(\frac{1}{|\vec{x} - \vec{x}_*|} + \frac{q}{\sqrt{(\vec{x} - \vec{x}_p)^2 + \epsilon^2}} \right) \quad (14)$$

⁴ Unless otherwise indicated, we work hereafter in code units: $GM_* = a = 1$ (which implies $\Omega_0 = 1$), where the variables have their usual meanings. Note that we also set our background surface density $\Sigma_0 = 1$, which nominally implies a disk mass comparable to the stellar mass; but our code ignores self-gravity and therefore all of our results for torques, \dot{e} , and \dot{a} simply scale as Σ_0 .

where $q = M_p/M_*$ is the planet-to-star mass ratio and $\epsilon = 0.5h$ is a smoothing length. The positions of the planet $\vec{x}_p(t)$ and star $\vec{x}_*(t)$ are found by solving Kepler's equation for an eccentric orbit using a Newton-Raphson root-finding scheme. Both planet and star are moved explicitly in time, keeping the center of mass fixed at $r = 0$. Accretion onto the planet is not modeled.

Standard model parameters are $\{q, \alpha, \mathcal{M}\} = \{0.001, 0.002, 28\}$. We also vary each of these 3 parameters separately to values above and below their standard value, generating an extra 6 models to explore parameter space.

3.2. Calculating \dot{e} Numerically

The planet lives on a fixed eccentric orbit of semimajor axis a and eccentricity e (Figure 1). The code is run until the disk surface density relaxes to a pattern that varies repeatedly and consistently with the planet's epicyclic motion; typically this takes thousands of planetary orbits (see Figure 2). The time derivative of eccentricity is time-averaged and recorded as a function of the chosen eccentricity, $\dot{e}(e)$.

The instantaneous value of \dot{e} follows from the definitions of the planet's orbital angular momentum and energy:

$$L = a^2 \Omega_0 M_p \sqrt{1 - e^2} \quad (15)$$

$$E = -\frac{1}{2} a^2 \Omega_0^2 M_p. \quad (16)$$

Combining the time derivatives of these two quantities (and remembering that $\Omega_0 = \sqrt{GM_*/a^3}$ depends on a) yields

$$\frac{\dot{e}}{e} = \frac{P(1 - e^2) - \Omega_0 T \sqrt{1 - e^2}}{\Omega_0^2 a^2 M_p e^2} \quad (17)$$

where T and P are the torque and power delivered to the planet, respectively:

$$T = \dot{L} = r F_\theta \quad (18)$$

$$P = \dot{E} = \vec{F} \cdot \vec{v}_p. \quad (19)$$

The planet's velocity is \vec{v}_p and the disk's gravitational force on the planet is

$$\vec{F} = GM_p \sum_{\text{zone } j} \frac{\Sigma dA_j}{(\vec{x}_j - \vec{x}_p)^2 + \epsilon^2} \hat{l}, \quad (20)$$

where \hat{l} is the unit vector pointing from the planet to the grid cell of area dA_j . The planet's migration rate can also be calculated via

$$\frac{\dot{a}}{a} = \frac{2P}{\Omega_0^2 a^2 M_p}. \quad (21)$$

4. RESULTS

Results are first presented for our standard model of a Jupiter-mass planet ($q = 10^{-3}$) in a disk with $h/a = 0.036$ ($\mathcal{M} = 28$) and $\tilde{\nu} = \nu/(a^2 \Omega_0) = \alpha/\mathcal{M}^2 = 2.5 \times 10^{-6}$ ($\alpha = 2 \times 10^{-3}$). Figure 2 displays the time derivative of eccentricity as a function of the eccentricity, $\dot{e}(e)$.

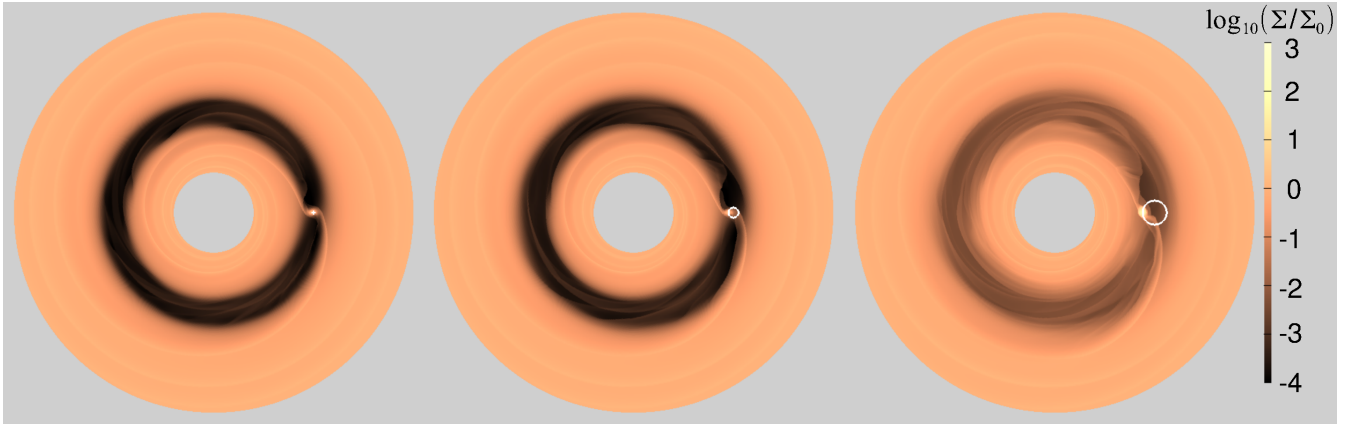


FIG. 1.— Standard disk-planet system employed in this study: $q = 10^{-3}$, $\tilde{\nu} = \nu/(a^2\Omega_0) = 2.5 \times 10^{-6}$, $\mathcal{M} = 28$ (equivalently, $h/a = 0.036$). The three panels correspond to three choices of planet eccentricity: $e = 0.01, 0.05$, and 0.12 , from left to right. White circles indicate the planet's approximate epicycle. The surface density inside the gap starts as low as $\Sigma_{\text{gap}}/\Sigma_0 \simeq 3 \times 10^{-4}$ at $e = 0.01$ and increases with increasing e . Eccentricity damps for $e = 0.01$; amplifies for $e = 0.05$; and damps for $e = 0.12$.

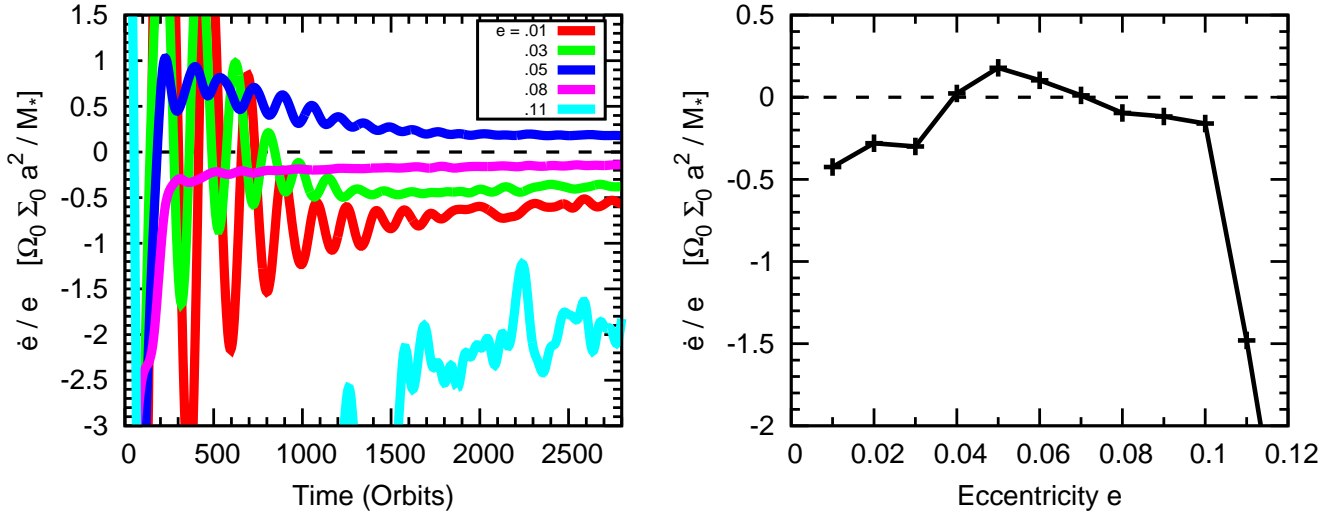


FIG. 2.— Time derivative of eccentricity as a function of eccentricity for our standard model parameters. *Left*: \dot{e}/e as a running average over time, demonstrating convergence. *Right*: Final time-averaged \dot{e}/e as a function of e . Eccentricity is damped for $e < e_{\min} \simeq 0.04$; excited for $e_{\min} < e < e_{\max} \simeq 0.07$; and damped for $e > e_{\max}$. Thus, there are two attractors: $e = 0$ and $e = e_{\max}$. Eccentricity damping is particularly strong at $e > 0.1$ when the planet collides into the gap walls.

The left panel shows the running time average of \dot{e}/e , demonstrating that it can take many thousands of orbits to achieve a quasi-steady state (not surprising given the low viscosity). The right panel shows the asymptotic value of \dot{e}/e , as a function of e .

Some highlights from Figure 2:

- For intermediate eccentricities, $\dot{e} > 0$: Jupiter-mass planets can, under certain circumstances, have their eccentricities excited by the disk.
- As $e \rightarrow 0$, $\dot{e} < 0$. Thus $e = 0$ is an attractor of the system for small e .
- Eccentricity excitation occurs only for $e > e_{\min} \simeq 0.04$: this is a finite-amplitude instability, as predicted by GS03.
- As e increases, eccentricity eventually damps. The value $e_{\max} \simeq 0.07$ is a second attractor, relevant for $e > e_{\min}$.

- For the largest values of e considered, \dot{e} plunges to large negative values. Here the planet's epicyclic motion causes it to collide with the gap walls (see also Figure 1); the gap fills up and eccentricity strongly damps.

Figure 3 plots the migration rate \dot{a}/a for our standard model. Note that in contrast with \dot{e} , the migration rate does not depend sensitively on e , at least until $e \gtrsim w/a \simeq 0.1$ and the planet crashes into the gap walls. The substantial damping of eccentricity for $e \gtrsim w/a$ found in Figure 2 coincides with a large, positive migration rate in Figure 3, similar to what was observed in the live-planet study of D'Angelo et al. (2006). However, it should be emphasized that this fast outward migration is only sustained as long as the eccentricity is this large. In reality the eccentricity should be quickly damped to $e = e_{\max} \simeq 0.07$ (Figure 2), whereupon $\dot{a} < 0$ as usual.

Figure 4 shows the gap depth $\Sigma_{\text{gap}}/\Sigma_0$ for this system. Gap depth is computed by calculating the azimuthally averaged and time-averaged surface density as a function

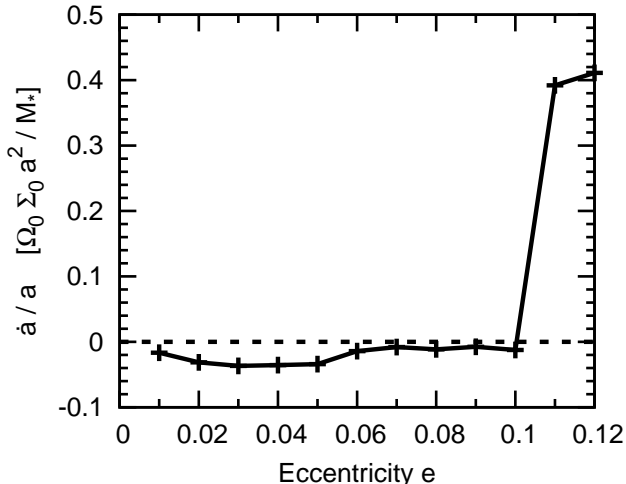


FIG. 3.— Migration rates as a function of eccentricity for our standard model. For modest eccentricities, \dot{a} is negative and roughly independent of e . Once the planet collides with the gap walls, \dot{a} becomes large and positive. The fast outward migration coincides with the large negative \dot{e} seen in Figure 2.

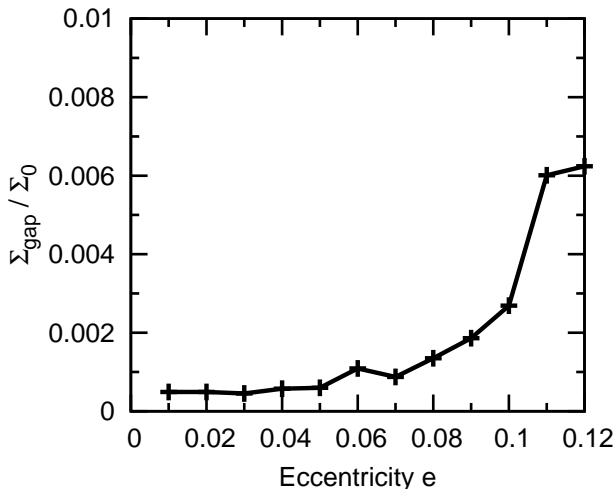


FIG. 4.— Gap depth $\Sigma_{\text{gap}}/\Sigma_0$ is computed as a function of eccentricity. Depths are calculated by averaging $\Sigma(r)$ azimuthally and over time, excising from the azimuthal average a region of radius $0.2a$ centered on the planet’s guiding center. The minimum of this averaged $\Sigma(r)$ gives Σ_{gap} .

of radius, $\Sigma(r)$, and finding the minimum of this function. A region of radius $0.2a$ centered on the planet’s guiding center at $(r, \theta) = (a, \Omega_0 t)$ is excised from the azimuthal average, in order to avoid contamination from material very close to the planet. Increasingly eccentric planets have shallower gaps.

In the next section, we elaborate upon all the trends highlighted above. We apply the theory of disk-planet interactions pioneered by Goldreich & Tremaine (1980) to see if we can reproduce quantitatively the behavior of \dot{e} measured numerically.

4.1. Detailed Comparison with GS03 for Standard Model

Here we compare our numerical results for \dot{e} for our standard model with those from analytic theory. Using formulae derived by Goldreich & Tremaine (1980),

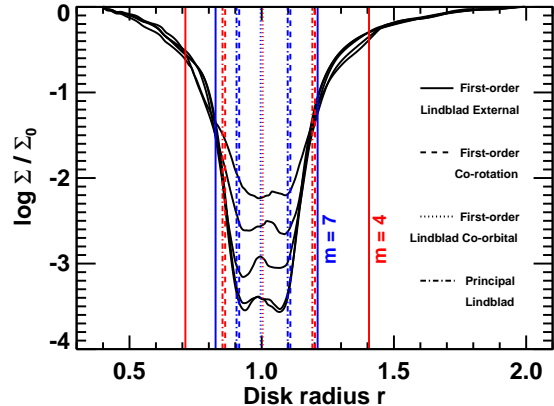


FIG. 5.— How gap profiles vary with e for our standard model. From bottom to top, surface density profiles correspond to $e = 0.01, 0.03, 0.06, 0.10$, and 0.12 . Each profile is azimuthally averaged from a late-time snapshot excised of a circular region of radius $= 0.2a$ centered on $(r, \theta) = (a, \Omega_0 t)$; the excision removes the highly overdense material in the planet’s immediate vicinity from the azimuthal average. Resonances from two of the more significant wavenumbers (as judged from Figure 7) are plotted. What appear to be nearly overlapping resonances in the figure actually do completely overlap in their nominal positions (e.g., the $m = 4$ principal Lindblad and $m = 4$ first-order co-rotation resonances); we plot these overlapping resonances with small arbitrary offsets for visual clarity only. The co-orbital resonances are so named because they are located at the planet’s semi-major axis ($r = a$); they should not be confused with the co-rotation resonances, which are offset from $r = a$ because they co-rotate with a particular term in the planet’s Fourier-expanded potential whose pattern speed does not in general equal the planet’s mean motion.

Ward (1988), Papaloizou & Larwood (2000), and Ogilvie & Lubow (2003), we compute the contributions to \dot{e} from various kinds of resonances: principal Lindblad resonances, first-order (as expanded in the planet’s eccentricity) Lindblad resonances, and first-order co-rotation resonances. Principal co-rotation resonances are omitted from our analysis, as these depend on $d\Sigma/dr$ at the very gap center; this derivative (difficult to calculate reliably) is assumed to be negligibly small for our deep gaps.

The formulae for \dot{e} are given in the Appendix. They depend on surface density $\Sigma(r)$ and its slope $d\Sigma(r)/dr$; these two quantities are read directly off snapshots of the numerical solution, so in this sense our calculation is semi-analytic.⁵ A sampling of surface density profiles $\Sigma(r)$ vs. e is provided in Figure 5, overlaid with the locations of some of the more important resonances. Each surface density profile is taken from an individual snapshot in time, azimuthally averaged after excising a circular region of radius $= 0.2a$ centered on the planet’s guiding center at $(r, \theta) = (a, \Omega_0 t)$. The excised region contains large and highly time-variable overdensities in the immediate vicinity of the planet that the analytic theories—which govern small disturbances on a smooth background—were not intended to treat. We will see at the end of this section that torques from this excised region are significant in some regions of parameter space.

The contributions to \dot{e} from the various resonances are dissected in Figure 6 (top panel). As anticipated by

⁵ In the case of a gapless disk ($\Sigma = \Sigma_0$), the equations in the Appendix give a value for $\dot{e}/e < 0$ that matches that of equation (5) to within $\sim 20\%$, after adjusting the strength of the softening term in the generalized Laplace coefficient.

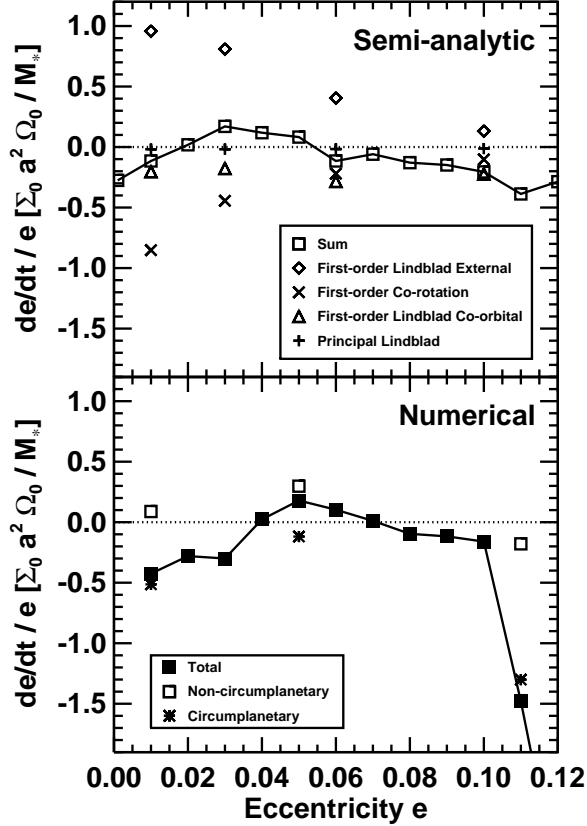


FIG. 6.— Disentangling the web of resonances that contribute to eccentricity evolution for our standard disk model. *Top*: \dot{e}/e as computed semi-analytically from the formulae in the Appendix, evaluated using the azimuthally averaged surface density profiles $\Sigma(r)$ from our numerical calculations (Figure 5). For $e = 0.01$, we employ $\Sigma(r)$ as computed for $e = 0.1$, since the surface density profiles do not change much for $e \leq 0.03$. *Bottom*: \dot{e}/e computed wholly numerically, with contributions from circumplanetary (within 1 Hill radius) and non-circumplanetary material distinguished for a few sample e 's. The semi-analytic calculation exhibits two trends: (1) a rise in \dot{e}/e at small e accompanied by a zero crossing that reflects the saturation of first-order co-rotation resonances and the growing dominance of first-order Lindblad external resonances; and (2) a drop in \dot{e}/e at large e accompanied by a second zero crossing that reflects the weakening of Lindblad resonances from the planet's increasingly supersonic epicyclic motion. These behaviors appear qualitatively reproduced by the numerical calculations, with modifications introduced by circumplanetary torques that linear theory does not capture. The huge drop in \dot{e} at $e \geq 0.11$ arises from the planet careening into the gap walls.

GS03, the strongest resonances are the first-order Lindblad external resonances which excite e , and the first-order co-rotation resonances which damp e . The first-order Lindblad co-orbital resonances also damp e , but are weaker because they are situated in the dead center of the gap where surface densities are at their lowest. Principal Lindblad resonances contribute negligibly to \dot{e} . Figure 7 shows that wavenumbers $m \simeq 2-8$ contribute most to \dot{e} ; contributions from higher m , up to our assumed cut-off at $m_{\max} = \mathcal{M}/2$, are less important.

The broad similarity between our semi-analytic calculation (Figure 6, top panel) and our numerical results (Figure 6, bottom panel) emboldens us to give the following interpretation of the dynamics. As e increases from 0, \dot{e} switches from negative to positive. This first zero cross-

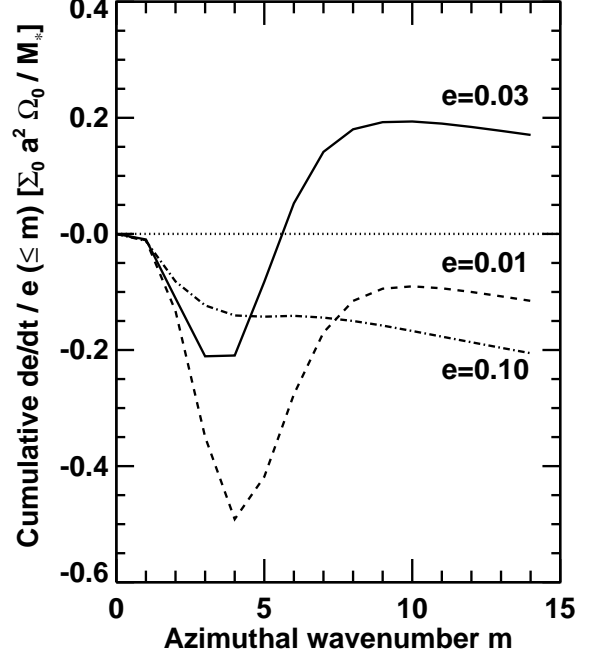


FIG. 7.— Running sum of \dot{e}/e vs. azimuthal wavenumber m for our standard disk model parameters, calculated semi-analytically. Contributions from all kinds of resonances (see Figure 6) are totaled for every m . The sum is truncated at $m_{\max} = \mathcal{M}/2 = 14$ to crudely account for the “torque cut-off” (Goldreich & Tremaine 1980). Most of the contributions to \dot{e}/e arise from $m \simeq 2-8$. The locations of the various resonances for $m = 4$ and $m = 7$ are shown in Figure 5.

ing is the finite-amplitude instability of GS03 and Ogilvie & Lubow (2003). The instability results because the first-order co-rotation resonances (which damp e) weaken from increasing saturation with increasing e . Evidence for this saturation can be seen in Figure 5, where surface density gradients are shallower for higher eccentricities at the locations of $m = 4-7$ first-order co-rotation resonances; the flattening of surface density is more easily seen at smaller orbital radii $r < 1$. Above a threshold e , the co-rotation resonances give way to the first-order Lindblad external resonances which render \dot{e} positive in the net. Further increases in e , however, bring \dot{e} back down to a second zero crossing. The external resonances weaken as e exceeds h/a , i.e., as the planet's epicyclic motion becomes supersonic (Papaloizou & Larwood 2000). The consequence of this supersonic weakening with increasing e is that the first-order co-rotation resonances—which are unaffected by supersonic motion—and the first-order Lindblad co-orbital resonances regain the upper hand at large e to make $\dot{e} < 0$. Although the co-orbital Lindblads suffer from the same supersonic weakening as do the external Lindblads, the co-orbitals yield a (negative) value of \dot{e}/e that hardly varies with e ; their weakening is mitigated by the surface density at gap center which grows with e (Figures 4 and 5), maintaining the strength of the co-orbitals.

Perhaps the most glaring discrepancy between our semi-analytic and numerical results is at the largest values of e . Numerically, at $e \geq 0.11$, we find eccentricity damping rates that are substantially higher than those expected from theory. As the bottom panel of Figure 6

indicates, the large negative values of \dot{e}/e are generated from torques exerted by “circumplanetary” material—here defined as material within 1 Hill radius of the planet’s instantaneous position (the circumplanetary region so defined is a subset of the excised region used to calculate azimuthal averages of surface density). The dominance of circumplanetary torques is not surprising at large e : the epicyclic motion is so wide that the planet collides with the gap walls and suffers dynamical friction from high density gas. What is surprising is that circumplanetary torques also dominate at the smallest value of $e = 0.01$, rendering \dot{e} more negative than expected from theory and pushing the onset of the eccentricity instability to larger $e \simeq 0.04$ (Figure 6, bottom panel). The properties of the circumplanetary region are uncertain and cannot be reliably predicted from linear theory. In our numerical calculations, details of the circumplanetary flow are subject to such issues as grid resolution, smoothing length, and prescriptions for how the planet accretes.

4.2. Dependence on Disk and Planet Parameters

Figure 8 shows results for $\dot{e}(e)$ for our six disk-planet systems scattered across parameter space. The observed changes to $\dot{e}(e)$ are complicated and difficult to follow in detail. We performed the same semi-analytic analysis for these models as we did for our standard model (Section 4.1), and were able to reproduce only some of the trends documented in Figure 8. Part of our difficulty stemmed from circumplanetary torques which often proved significant, and which we could not evaluate using the standard analytic theory.

Broadly speaking, however, we can say that $\dot{e} > 0$ favors high-mass planets, thin disks, and low viscosities—these cases are highlighted in red in Figure 8.

Qualitatively, the circumstances that lead to $\dot{e} > 0$ are the same ones that produce deep gaps. Gap depths are gauged by the dimensionless parameter

$$K(q, \alpha, h/a) = \frac{q^2}{\alpha(h/a)^5}. \quad (22)$$

(Duffell & MacFadyen 2013; Fung et al. 2014; Kanagawa et al. 2015; Duffell 2015) and it is interesting to ask whether this same parameter can predict eccentricity growth. Figure 9 lists values of K for our seven disk-planet parameter studies, together with K -values from previous studies of eccentricity evolution. A rough threshold of $K \sim 10^3$ – 10^4 dividing $\dot{e} < 0$ from $\dot{e} > 0$ can be discerned—equivalent to a threshold gap depth $\Sigma_{\text{gap}}/\Sigma_0 \sim 10^{-3}$.

4.3. Gap Widths

The width of a gap opened by a planet gives a hard upper bound on the eccentricity that can be excited by hard torques. As such, it is worthwhile understanding how the gap width w depends on input parameters.

The exercise performed in Section 2 predicts that $w/a \sim (q^2/\tilde{\nu})^{1/3}$. This relation is tested in Figure 10 where gap half-widths are plotted against the dimensionless parameter $q^2/\tilde{\nu}$. The gap half-width is evaluated by differencing the radii at which $\Sigma = 0.1\Sigma_0$ and dividing by two. The data in Figure 10 appear to conform to a power law, but with a somewhat shallower slope than the

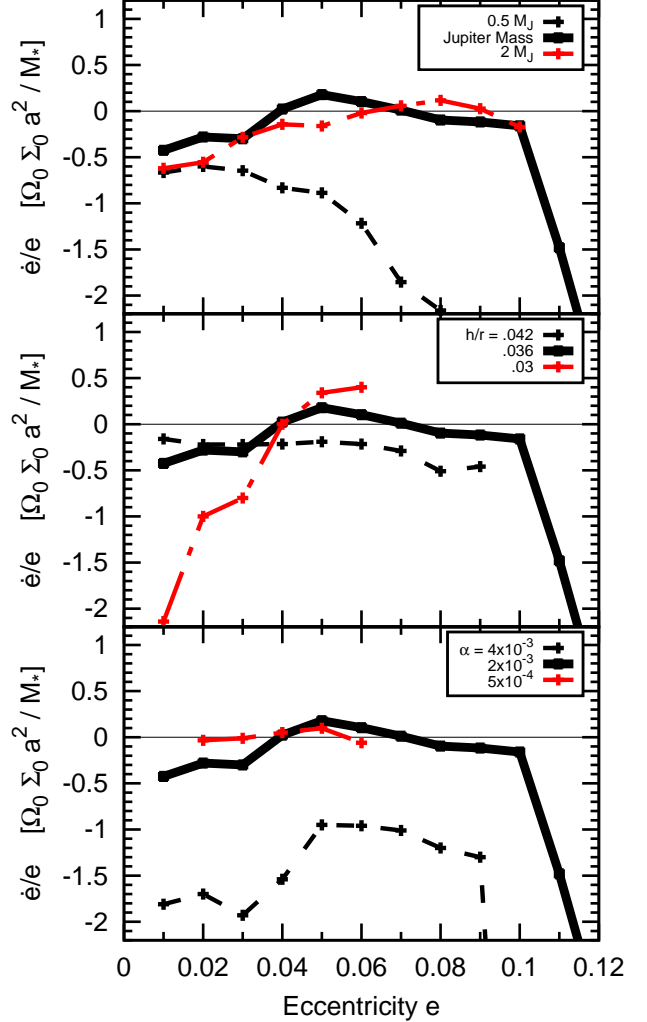


FIG. 8.— How \dot{e}/e varies across parameter space. Data are plotted only for those models whose running time-averages of \dot{e}/e converged to well-defined values; disks with especially low h/a or low α perturbed by planets with high eccentricity exhibited strong instabilities and failed to give convergent answers. Eccentricity driving favors large planet masses, small h/a , and small α , the same region of parameter space that produces deep gaps.

predicted $1/3$: $w/2a = 0.25(q^2/\tilde{\nu})^{0.22}$, where $w/2$ is the gap half-width.

For our standard model parameters, the above fitting formula gives $w/2a = 0.2$. By comparison, the eccentricity beyond which \dot{e} plummets to large negative values (see Figure 2) is $e = 0.11$; this is a factor of 2 smaller than $w/2a$ and suggests that in this context, a more relevant definition for gap half-width would be obtained by taking $\Sigma/\Sigma_0 = 10^{-3}$ rather than $\Sigma/\Sigma_0 = 10^{-1}$ —see Figure 5.

We close with the reminder that the actual value to which a planet’s eccentricity relaxes is not given by the gap-collision value, but rather by e_{max} (which for our standard model equals 0.07)—this is the value for which $\dot{e} = 0$, and marks where supersonically weakened external Lindblad resonances balance co-rotation and co-orbital Lindblad resonances (Section 4.1).

5. SUMMARY AND DISCUSSION

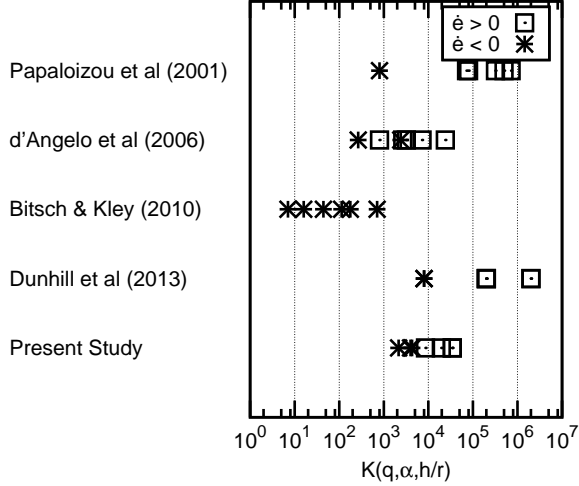


FIG. 9.— Several studies of planet-disk eccentricity evolution are compared using the parameter $K \equiv q^2 \mathcal{M}^5 / \alpha$, which governs gap depths (Duffell & MacFadyen 2013; Fung et al. 2014). A rough correlation between high $K \gtrsim 10^3$ – 10^4 (deep gaps having $\Sigma_{\text{gap}}/\Sigma_0 \lesssim 10^{-3}$) and $\dot{e} > 0$ can be discerned.

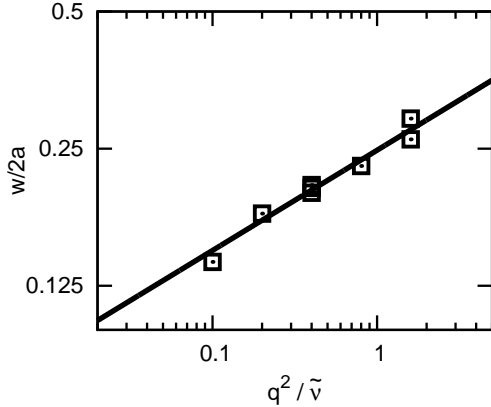


FIG. 10.— Gap half-widths $w/2a$ (defined as half the distance between points in the gap where $\Sigma/\Sigma_0 = 0.1$) increase with increasing planet-to-star mass ratio q and decreasing disk viscosity $\tilde{\nu}$. Equation (3) predicts that $w/2a \sim (q^2/\tilde{\nu})^{1/3}$; our measurements are fitted by $w/2a \simeq 0.25(q^2/\tilde{\nu})^{0.22}$ (solid line). The gap half-width gives a hard upper bound on eccentricities that can be sustained by planets embedded in their natal gas disks. The actual bound e_{max} on e is somewhat smaller — of order a few times h/a — and occurs when supersonically-weakened external resonances exactly cancel co-orbital and co-rotation resonances to render $\dot{e} = 0$.

This study demonstrates that Jupiter-mass planets can have their orbital eccentricities amplified by disk torques — provided they open deep enough gaps, and provided their eccentricities exceed a threshold value. The finite-amplitude instability documented here appears to be the same as that predicted analytically by Goldreich & Sari (2003). Eccentricities are damped by first-order co-orbital Lindblad torques and first-order co-rotation torques. Deep gaps are required to disable the former, while finite eccentricities serve to saturate (i.e., weaken)

the latter (Ogilvie & Lubow 2003). With these requirements met, first-order external Lindblad resonances can excite a planet’s eccentricity.

Our results are similar to those of D’Angelo et al. (2006) who also found eccentricity growth for Jovian-mass planets at low disk viscosities ($\alpha \sim 10^{-3}$), but differ from them insofar as the eccentricity growth that we report explicitly requires a non-zero initial eccentricity. Other studies did not find eccentricity growth for Jupiter-mass planets but used larger viscosities or thicker disks. Their results may be reconciled with ours by examining the parameter $K \equiv q^2 \mathcal{M}^5 / \alpha$ which governs gap depth. Eccentricity driving seems to require large $K \gtrsim 10^3$ – 10^4 , i.e., deep gaps of surface density $\Sigma_{\text{gap}}/\Sigma_0 \sim 1/K$.

Eccentricities do not amplify without bound. As eccentricities increase above the disk aspect ratio h/a — i.e., as the planet’s epicyclic motion becomes supersonic — the external resonances weaken (Papaloizou & Larwood 2000). At the same time, the co-orbital resonances strengthen with increasing eccentricity as more disk material leaks into the gap. Consequently, eccentricity damps above a certain value that scales like h/a ; this value is an attractor for the system. In our numerical experiments, the attractor eccentricity ranges from 0.07 to 0.09. At still larger eccentricities — so large that the planet collides into gap walls separated by a fractional width w/a — the damping of eccentricity becomes catastrophically rapid.

The results of our numerical study align with analytic expectations only broadly. Significant torques are exerted by material within a Hill sphere or so of the planet that linear theory cannot capture. Modeling circumplanetary flows is technically challenging and we do not claim to have gotten it right. In addition to the usual worries about smoothing lengths and planetary accretion prescriptions, there looms the possibility that flows in 3D could look qualitatively different from our 2D solutions (Ormel et al. 2015). In particular, gaps may be systematically shallower and co-rotation resonances might never saturate (Fung et al. 2015).

The eccentricity driving reported here does not rely on non-barotropic (i.e., non-isothermal or non-adiabatic) thermodynamics, as our numerical calculations are for strictly isothermal disks. Including non-barotropic effects such as those introduced by external irradiation of gap walls may help to lower the threshold eccentricity for instability (Tsang et al. 2014). If eccentricity driving survives in 3D, it offers a possible explanation for the low-to-moderate eccentricities $\lesssim 0.1$ observed for giant planets—including Jupiter and conceivably Saturn—without recourse to planet-planet interactions (cf. Tsiganis et al. 2005).

Computational resources were provided by NASA’s High-End Computing (HEC) Program administered by the NASA Advanced Supercomputing (NAS) Division at Ames Research Center. Financial support was provided by the Theoretical Astrophysics Center and the Center for Integrative Planetary Science at UC Berkeley, and by grants to EC from the NASA Origins and NASA Outer Planets programs. We are grateful to Rebekah Dawson, Alex Dunhill, Re’em Sari, and Taku Takeuchi for helpful discussions.

REFERENCES

- Bitsch, B., & Kley, W. 2010, A&A, 523, A30
 Butler, R. P., Wright, J. T., Marcy, G. W., et al. 2006, ApJ, 646, 505
 Cresswell, P., Dirksen, G., Kley, W., & Nelson, R. P. 2007, A&A, 473, 329
 Cresswell, P., & Nelson, R. P. 2006, A&A, 450, 833
 D’Angelo, G., Lubow, S. H., & Bate, M. R. 2006, ApJ, 652, 1698
 Dawson, R. I., & Chiang, E. 2014, Science, 346, 212
 Duffell, P. C. 2015, ApJ, 807, L11
 Duffell, P. C., & MacFadyen, A. I. 2011, ApJS, 197, 15
 —. 2012, ApJ, 755, 7
 —. 2013, ApJ, 769, 41
 Dunhill, A. C., Alexander, R. D., & Armitage, P. J. 2013, MNRAS, 428, 3072
 Fung, J., Artymowicz, P., & Wu, Y. 2015, ArXiv e-prints, arXiv:1505.03152
 Fung, J., Shi, J.-M., & Chiang, E. 2014, ApJ, 782, 88
 Goldreich, P., & Sari, R. 2003, ApJ, 585, 1024
 Jurić, M., & Tremaine, S. 2008, ApJ, 686, 603
 Kanagawa, K. D., Tanaka, H., Muto, T., Tanigawa, T., & Takeuchi, T. 2015, MNRAS, 448, 994
 Li, H., Lubow, S. H., Li, S., & Lin, D. N. C. 2009, ApJ, 690, L52
 Marcy, G., Butler, R. P., Fischer, D., et al. 2005, Progress of Theoretical Physics Supplement, 158, 24
 Ormel, C. W., Shi, J.-M., & Kuiper, R. 2015, MNRAS, 447, 3512
 Papaloizou, J. C. B., Nelson, R. P., & Masset, F. 2001, A&A, 366, 263
 Takeda, G., & Rasio, F. A. 2005, ApJ, 627, 1001
 Tsang, D., Turner, N. J., & Cumming, A. 2014, ApJ, 782, 113
 Tsiganis, K., Gomes, R., Morbidelli, A., & Levison, H. F. 2005, Nature, 435, 459
 Ward, W. R. 1988, Icarus, 73, 330
 Wu, Y., & Lithwick, Y. 2011, ApJ, 735, 109
 Yu, C., Li, H., Li, S., Lubow, S. H., & Lin, D. N. C. 2010, ApJ, 712, 198
 Zakamska, N. L., Pan, M., & Ford, E. B. 2011, MNRAS, 410, 1895

We make no accounting for changes in resonance location from disk pressure gradients or self-gravity.

The planet’s eccentricity changes at the rate

$$\dot{e} = -\frac{\Omega_{\text{planet}}}{m} \frac{H_{\text{planet}}^2}{(GM_*)^2} \frac{T_{m+1,m}^L}{eM_{\text{planet}}^3} \times \frac{1}{1 + 0.25(e\mathcal{M})^3}. \quad (\text{A4})$$

The second factor involving the Mach number $\mathcal{M} \equiv a_{\text{planet}}/h$ is taken from Papaloizou & Larwood (2000, their equation 32), and accounts for how Lindblad torques weaken as the planet’s epicyclic motion becomes increasingly supersonic. The first-order Lindblad torque equals

$$T_{m+1,m}^L = -m\pi^2\Sigma \left(r \frac{dD}{dr}\right)^{-1} \times \left(r \frac{d\phi_{m+1,m}}{dr} + \frac{2\Omega}{\Omega - \Omega_{m+1,m}} \phi_{m+1,m}\right)^2 \quad (\text{A5})$$

where

$$r \frac{dD}{dr} = -3\Omega^2 + 3\Omega m^2 \left(\Omega - \frac{m+1}{m} \Omega_{\text{planet}}\right). \quad (\text{A6})$$

All quantities are evaluated at the resonance location (either equation A2 or A3). The surface density Σ is interpolated from the azimuthally averaged density profile of an excised snapshot (see Figure 5 and related text for details). The potential amplitude is given by

$$\phi_{m+1,m} = -\frac{GM_{\text{planet}}e}{a_{\text{planet}}} \times \left[\left(\frac{1}{2} + m + \frac{\beta}{2} \frac{d}{d\beta}\right) b_{1/2}^m(\beta) - 2\beta\delta_{m,1}\right] \quad (\text{A7})$$

where $\delta_{m,1}$ is the Kronecker delta. Note that $r d/dr = \beta d/d\beta$. The Laplace coefficient is

$$b_{1/2}^m(\beta) = \frac{2}{\pi} \int_0^\pi \frac{\cos m\phi}{(1 - 2\beta \cos \phi + \beta^2 + 2/\mathcal{M}^2)^{1/2}} d\phi \quad (\text{A8})$$

and is evaluated numerically. The factor of $2/\mathcal{M}^2$ accounts roughly for how the planet’s point-mass potential is softened by length $\sim h$ (cf. Ward 1988). The coefficient of 2 is obtained by calibrating our final answer for \dot{e}/e for the test case of a gapless ($\Sigma = \Sigma_0$) disk to match

APPENDIX

SEMI-ANALYTIC CALCULATION OF \dot{e}/e

We list here the formulae used to evaluate \dot{e} and make Figures 6 and 7. We let a_{planet} be the planet’s semi-major axis (this is the same variable as a in the main text), e the planet’s eccentricity, M_* the stellar mass, and G the gravitational constant. We further define $H_{\text{planet}} = M_{\text{planet}} \sqrt{GM_* a_{\text{planet}} (1 - e^2)}$ to be the planet’s orbital angular momentum and $\Omega_{\text{planet}} = \sqrt{GM_*/a_{\text{planet}}^3}$ to be the planet’s orbital angular frequency. In all our numerical evaluations, $GM_* = a_{\text{planet}} = \Omega_{\text{planet}} = 1$. The disk semi-major axis is r .

We account for eight kinds of resonances: all those considered in Table 1 of Goldreich & Sari (2003) with the exception of the principal co-rotation resonance. For every resonance type, we give the full set of equations required to compute \dot{e} . Some of the equations are shared between types, but we list the complete set anyway under each type for ease of reference.

First-order Lindblad resonances
 with $\ell = m + 1$

The pattern speed of the potential component with $\ell = m + 1$ where m is the azimuthal wavenumber (see Goldreich & Tremaine 1980 for their Fourier notation) is given by

$$\Omega_{m+1,m} = \left(\frac{m+1}{m}\right) \Omega_{\text{planet}}. \quad (\text{A1})$$

There are two Lindblad resonances associated with this potential: a “co-orbital” resonance so called because it is located at the planet’s semi-major axis:

$$\left. \begin{aligned} \beta \equiv r/a_{\text{planet}} &= 1 \\ \Omega &= \Omega_{\text{planet}} \end{aligned} \right\} \text{co-orbital} \quad (\text{A2})$$

and an “external” resonance:

$$\left. \begin{aligned} \beta &= \left(\frac{m-1}{m+1}\right)^{2/3} \\ \Omega &= \left(\frac{m+1}{m-1}\right) \Omega_{\text{planet}} \end{aligned} \right\} \text{external}. \quad (\text{A3})$$

approximately the value given by equation (5); adopting a smaller coefficient would overestimate the strength of the co-orbital resonances and lead to excessively negative values of \dot{e} .

Equation A4 is summed from $m_{\min} = 1$ to $m_{\max} = \mathcal{M}/2$, where m_{\max} crudely approximates the torque cut-off (Goldreich & Tremaine 1980). For $m = 1$ the external resonance does not exist.

First-order Lindblad resonances
with $\ell = m - 1$

This case is analogous to the one above. The sum runs from $m_{\min} = 2$ to $m_{\max} = \mathcal{M}/2$.

$$\Omega_{m-1,m} = \left(\frac{m-1}{m}\right) \Omega_{\text{planet}} \quad (\text{A9})$$

$$\Omega = \Omega_{\text{planet}} \left. \begin{array}{l} \beta = 1 \\ \end{array} \right\} \text{co-orbital} \quad (\text{A10})$$

$$\Omega = \left(\frac{m-1}{m+1}\right) \Omega_{\text{planet}} \left. \begin{array}{l} \beta = \left(\frac{m+1}{m-1}\right)^{2/3} \\ \end{array} \right\} \text{external} \quad (\text{A11})$$

$$\dot{e} = + \frac{\Omega_{\text{planet}}}{m} \frac{H_{\text{planet}}^2}{(GM_*)^2} \frac{T_{m-1,m}^L}{eM_{\text{planet}}^3} \times \frac{1}{1 + 0.25 (e\mathcal{M})^3} \quad (\text{A12})$$

$$T_{m-1,m}^L = -m\pi^2 \Sigma \left(r \frac{dD}{dr} \right)^{-1} \times \left(r \frac{d\phi_{m-1,m}}{dr} + \frac{2\Omega}{\Omega - \Omega_{m-1,m}} \phi_{m-1,m} \right)^2 \quad (\text{A13})$$

$$r \frac{dD}{dr} = -3\Omega^2 + 3\Omega m^2 \left(\Omega - \frac{m-1}{m} \Omega_{\text{planet}} \right) \quad (\text{A14})$$

$$\phi_{m-1,m} = -\frac{GM_{\text{planet}} e}{a_{\text{planet}}} \times \left(\frac{1}{2} - m + \frac{\beta}{2} \frac{d}{d\beta} \right) b_{1/2}^m(\beta) \quad (\text{A15})$$

where $b_{1/2}^m(\beta)$ is given by A8.

First-order Co-rotation Resonances
with $\ell = m + 1$

The sum runs from $m_{\min} = 1$ to $m_{\max} = \mathcal{M}/2$.

$$\Omega_{m+1,m} = \left(\frac{m+1}{m}\right) \Omega_{\text{planet}} \quad (\text{A16})$$

$$\Omega = \left(\frac{m+1}{m}\right) \Omega_{\text{planet}} \left. \begin{array}{l} \beta = \left(\frac{m}{m+1}\right)^{2/3} \\ \end{array} \right\} \text{co-rotation} \quad (\text{A17})$$

$$\dot{e} = -\frac{\Omega_{\text{planet}}}{m} \frac{H_{\text{planet}}^2}{(GM_*)^2} \frac{T_{m+1,m}^C}{eM_{\text{planet}}^3} \times F(p) \quad (\text{A18})$$

The saturation factor is derived by Ogilvie & Lubow (2003) and fitted numerically by Goldreich & Sari (2003):

$$F(p) = \frac{(1 + 0.65p^3)^{5/6}}{(1 + 1.022p^2)^2} \quad (\text{A19})$$

$$p = \frac{2\phi_{m+1,m}}{3\Omega^2} \left(\frac{3\Omega m}{2\beta a_{\text{planet}} \nu} \right)^{2/3} \quad (\text{A20})$$

$$T_{m+1,m}^C = -\frac{4\pi^2 m}{3} \left(\frac{m}{m+1} \right)^2 \beta a_{\text{planet}} \Omega_{\text{planet}}^2 \times \phi_{m+1,m}^2 \left(\frac{d\Sigma}{dr} + \frac{3}{2} \frac{\Sigma}{r} \right) \quad (\text{A21})$$

$$\phi_{m+1,m} = -\frac{GM_{\text{planet}} e}{a_{\text{planet}}} \times \left[\left(\frac{1}{2} + m + \frac{\beta}{2} \frac{d}{d\beta} \right) b_{1/2}^m(\beta) - 2\beta \delta_{m,1} \right] \quad (\text{A22})$$

where $b_{1/2}^m(\beta)$ is given by A8.

First-order Co-rotation Resonances
with $\ell = m - 1$

The sum runs from $m_{\min} = 2$ to $m_{\max} = \mathcal{M}/2$.

$$\Omega_{m-1,m} = \left(\frac{m-1}{m}\right) \Omega_{\text{planet}} \quad (\text{A23})$$

$$\Omega = \left(\frac{m-1}{m}\right) \Omega_{\text{planet}} \left. \begin{array}{l} \beta = \left(\frac{m}{m-1}\right)^{2/3} \\ \end{array} \right\} \text{co-rotation} \quad (\text{A24})$$

$$\dot{e} = + \frac{\Omega_{\text{planet}}}{m} \frac{H_{\text{planet}}^2}{(GM_*)^2} \frac{T_{m-1,m}^C}{eM_{\text{planet}}^3} \times F(p) \quad (\text{A25})$$

$$F(p) = \frac{(1 + 0.65p^3)^{5/6}}{(1 + 1.022p^2)^2} \quad (\text{A26})$$

$$p = \frac{2\phi_{m-1,m}}{3\Omega^2} \left(\frac{3\Omega m}{2\beta a_{\text{planet}} \nu} \right)^{2/3} \quad (\text{A27})$$

$$T_{m-1,m}^C = -\frac{4\pi^2 m}{3} \left(\frac{m}{m-1} \right)^2 \beta a_{\text{planet}} \Omega_{\text{planet}}^2 \times \phi_{m-1,m}^2 \left(\frac{d\Sigma}{dr} + \frac{3}{2} \frac{\Sigma}{r} \right) \quad (\text{A28})$$

$$\phi_{m-1,m} = -\frac{GM_{\text{planet}} e}{a_{\text{planet}}} \times \left(\frac{1}{2} - m + \frac{\beta}{2} \frac{d}{d\beta} \right) b_{1/2}^m(\beta) \quad (\text{A29})$$

where $b_{1/2}^m(\beta)$ is given by A8.

Principal Inner Lindblad Resonances
with $\ell = m$

The sum runs from $m_{\min} = 1$ to $m_{\max} = \mathcal{M}/2$.

$$\Omega_{m,m} = \Omega_{\text{planet}} \quad (\text{A30})$$

$$\left. \begin{aligned} \beta &= \left(\frac{m}{m+1} \right)^{2/3} \\ \Omega &= \left(\frac{m+1}{m} \right) \Omega_{\text{planet}} \end{aligned} \right\} \text{inner} \quad (\text{A31})$$

$$\dot{e} = \frac{e\Omega_{\text{planet}}H_{\text{planet}}^2T_{m,m}^{\text{L}}}{2(GM_*)^2M_{\text{planet}}^3} \quad (\text{A32})$$

$$T_{m,m}^{\text{L}} = -m\pi^2\Sigma \left(r \frac{dD}{dr} \right)^{-1} \times \left(r \frac{d\phi_{m,m}}{dr} + \frac{2\Omega}{\Omega - \Omega_{m,m}} \phi_{m,m} \right)^2 \quad (\text{A33})$$

$$r \frac{dD}{dr} = -3\Omega^2 + 3\Omega m^2 (\Omega - \Omega_{\text{planet}}) \quad (\text{A34})$$

$$\phi_{m,m} = -\frac{GM_{\text{planet}}}{a_{\text{planet}}} \left(b_{1/2}^m(\beta) - \beta\delta_{m,1} \right) \quad (\text{A35})$$

where $b_{1/2}^m(\beta)$ is given by A8.

Principal Outer Lindblad Resonances
with $\ell = m$

The sum runs from $m_{\min} = 2$ to $m_{\max} = \mathcal{M}/2$.

$$\Omega_{m,m} = \Omega_{\text{planet}} \quad (\text{A36})$$

$$\left. \begin{aligned} \beta &= \left(\frac{m}{m-1} \right)^{2/3} \\ \Omega &= \left(\frac{m-1}{m} \right) \Omega_{\text{planet}} \end{aligned} \right\} \text{outer} \quad (\text{A37})$$

$$\dot{e} = \frac{e\Omega_{\text{planet}}H_{\text{planet}}^2T_{m,m}^{\text{L}}}{2(GM_*)^2M_{\text{planet}}^3} \quad (\text{A38})$$

$$T_{m,m}^{\text{L}} = -m\pi^2\Sigma \left(r \frac{dD}{dr} \right)^{-1} \times \left(r \frac{d\phi_{m,m}}{dr} + \frac{2\Omega}{\Omega - \Omega_{m,m}} \phi_{m,m} \right)^2 \quad (\text{A39})$$

$$r \frac{dD}{dr} = -3\Omega^2 + 3\Omega m^2 (\Omega - \Omega_{\text{planet}}) \quad (\text{A40})$$

$$\phi_{m,m} = -\frac{GM_{\text{planet}}}{a_{\text{planet}}} b_{1/2}^m(\beta) \quad (\text{A41})$$

where $b_{1/2}^m(\beta)$ is given by A8.